2025-sCO2.eu-178

# EXPERIMENTAL STUDY ON S-SHAPED FINS FOR HIGH HEAT FLUX COOLING WITH SUPERCRITICAL CO2

**Ryan Ghent**
Oxford Thermofluids Institute
Oxford, United Kingdom
Email: ry.ghent@gmail.com

**Zachary Jackson**
Oxford Thermofluids Institute
Oxford, United Kingdom

**Peter Ireland**
Oxford Thermofluids Institute
Oxford, United Kingdom

## ABSTRACT

High heat fluxes from nuclear fusion pose a challenge for heat exchange. Supercritical CO2 and micro-channel heat exchangers offer a way to solve this challenge, however heat transfer correlations for supercritical fluids do not necessarily carry over to higher heat fluxes. This experimental study investigates a promising geometry of S-Shaped fin micro-channel heat exchangers at heat fluxes up to 1 MW/m$^2$, 10 times hotter than previously tested in the literature. A high temperature test section was heated under laser diodes to represent the heat flux from fusion. A conjugate CFD study was performed, but this did not match the experimental temperatures well. To remedy this, an FE model was made, in which the heat transfer profile from CFD was scaled by a constant factor, giving better agreement with experimental temperatures. A thermal resistance network was developed, and the unknown heat transfer coefficient was varied to minimise the error between the predicted temperatures and experimental ones. This gave heat transfer coefficients that matched well with correlations in the literature, at these elevated heat fluxes. This implies that the design could be used effectively for the heat fluxes found in the blanket of a fusion reactor.

## 1. INTRODUCTION

Nuclear fusion has the potential to completely revolutionise power generation, allowing for near-limitless affordable energy [1]. Thermal management and heat exchange in the first wall of tokamak-type reactors is a key remaining challenge to this goal, with heat fluxes as large as 1 MW/m$^2$ in the blanket [2] at steady state, with transients in the divertor exceeding 50 MW/m$^2$. Pressure drops need to be small to efficiently capture energy from the fusion reactor and allow reactors to be viable at finite plasma gains.

Supercritical fluid properties vary strongly with temperature, as shown in Fig. 1. This allows for turbomachinery to be ten times smaller than for water [3], making supercritical a promising working fluid choice for fusion cooling. This is from the spike in heat capacity ($C_p$) at the pseudo-critical temperature ($T_{pc}$), and only a moderate reduction in density. Supercritical fluids can exhibit deterioration of heat transfer at high heat fluxes [4]. There is dependance on both geometry and orientation. As heat flux increases, the heat transfer coefficient (HTC) reaches a minimum and eventually returns to the original value. This makes supercritical fluids ideal for fusion blanket cooling, where the heat flux varies considerably, at least compared to traditional heat transfer fluids like water where the HTC does not recover until much higher temperature differences. The deterioration makes correlations unreliable at heat fluxes above the range they were developed for, as shown by the disagreement between correlations in [5] and [6] for the same geometry at different heat fluxes. This study will investigate the use of supercritical carbon dioxide, $sCO_2$, for fusion blanket cooling.

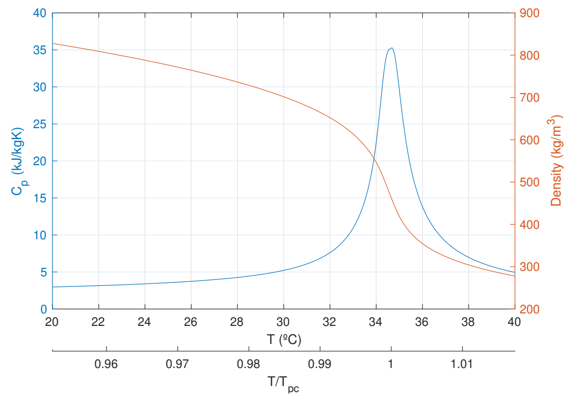


**Figure 1:** $sCO_2$ at 80 bar property variation against temperature and temperature divided by pseudo-critical temperature [7].

Micro-Channel Heat Exchangers (MCHEs) maximise surface area $A$ using small features with hydraulic diameter $D_\mathrm{h}$ < 1 mm , [8]. This allows for compact management of large heat fluxes. Different geometries of MCHE have dif-ferent heat transfer performance, as shown in Fig. 2. Of the main geometry types shown in Fig. 2, S-Fins have promis-ingly high heat transfer, and a friction factor over 4 times smaller than zig-zag channels [9].

S-shaped fins are a promising geometry for fusion cooling. However, they have not been tested with $sCO_2$ at fusion


DOI:10.17185/duepublico/83302

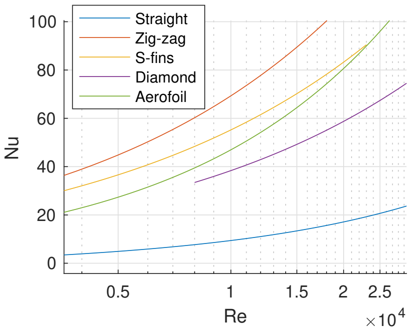


**Figure 2:** Heat transfer performance, as Nusselt number, of various MCHE geometries against Reynolds number. Curves for Nusselt number are generated using correlations found in: Zig-zag channels, S-Fin: [9]; Straight channels: [10]; Diamond fins: [11]; Aerofoil fins: [12]).

relevant heat fluxes. The deterioration of heat transfer at high heat fluxes means experimental work needs to be performed to extend current correlations for use in fusion.

S-shaped fins, Fig. 3, were originally proposed in [13], and optimised in [14]. The optimal shape was tested with $sCO_2$ in [9] using a counter-flow heat exchanger. Other sub-optimal variations were tested in a similar manner by the same group, between water and $sCO_2$ in [15] and [16]. The highest heat flux tested by this group was $0.05\ \mathrm{MW/m^2}$. The main aim of the group was to investigate generation IV fission reactors so this more than sufficed for their purposes. A more recent study [17] also did not use the optimal shape. This was also a counter-flow heat exchanger with water on both sides. The highest heat flux of this test was $0.1\ \mathrm{MW/m^2}$. As most magnetic confinement fusion reactors have blanket (that is heat exchange for power generation) heat fluxes of $1\ \mathrm{MW/m^2}$, this paper aims to study the geometry proposed by [9] at this higher heat flux.

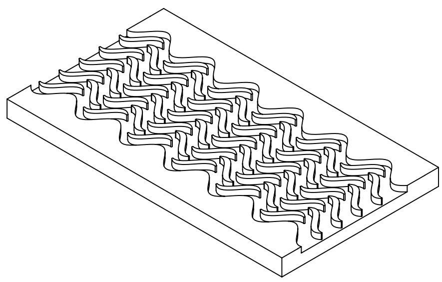

**Figure 3:** S-Fin geometry proposed in [13].

S-shaped fins have only been investigated up to heat fluxes of $0.1\ \mathrm{MW/m^2}$ [16], and using $sCO_2$, only up to $0.05\ \mathrm{MW/m^2}$ [9]. $sCO_2$ does not behave similarly at higher heat fluxes [4]. This paper investigates S-shaped fin PCHE at heat fluxes up to $1\ \mathrm{MW/m^2}$, typical heat fluxes for the blanket of fusion reactors [2].

This project aims to experimentally test a promising geometry of heat exchanger for use in blanket cooling for power generation.

## Nomenclature

**Greek Characters**

| | |
|---|---|
| $\alpha$ | Absorption |
| $\delta$ | Uncertainty in variable |
| $\mu$ | Dynamic viscosity (Pa s) |
| $\rho$ | Density $(\mathrm{kg/m^3})$ |

**Variables**

| | |
|---|---|
| $\dot{m}$ | Mass flow rate (kg/s) |
| $A$ | Surface Area $(\mathrm{m^2})$ |
| $C_\mathrm{p}$ | Specific heat capacity at constant pressure (J/kgK) |
| $G$ | Mass flux $(\mathrm{kg/m^2s})$ |
| $g(a,b)$ | $g$ as a function of $a$ and $b$ |
| $h$ | Heat transfer coefficient $(\mathrm{W/m^2K})$ |
| $i$ | Specific enthalpy (J/kg) |
| $k$ | Thermal conductivity (W/Km) |
| $P$ | Pressure (bar) |
| $Q$ | Heat (W) |
| $q$ | Heat flux $(\mathrm{W/m^2})$ |
| $T$ | Temperature (°C) |
| $V$ | Volume $(\mathrm{m^3})$ |

**Non-dimensional numbers**

| | |
|---|---|
| $f$ | Friction factor |
| $j$ | Stand-in dummy variable |
| Nu | Nusselt number |
| Pr | Prandtl number |
| Re | Reynolds number |

**Subscripts**

| | |
|---|---|
| b | Bulk fluid property |
| CFD | Computational Fluid Dynamics |
| exp. | Experimental data |
| FEM | Finite Element Model |
| in | Properties at inlet to the test piece |
| lit. | Literature |
| out | Properties at outlet to the test piece |
| pc | Pseudo-critical |
| TRN | Thermal Resistance Network |
| w | Wall property |

## 2. SUPERCRITICAL EXPERIMENTAL SETUP

This section details the experimental setup. A steel test piece was manufactured, laser modules used to apply the heat flux, and $sCO_2$ pumped through to cool it.

The main test section is shown in Fig 4. It is comprised of an 80 mm length of S-Fins and is approximately 52 mm wide. The first 30 mm, $\approx 20 \times D_\mathrm{h}$, are a development length, the next 40 mm directly heated, and the last 10 mm stop the exit header from affecting the heated section. Sinusoidal side walls were used to minimise impact on the flow field. (Refer to Fig. 3, and Annex A for more information on the shape of the fins used.)

MCHEs are normally manufactured by chemical etching a pattern into plates and then diffusion bonding these plates


DOI: 10.17185/duepublico/83302

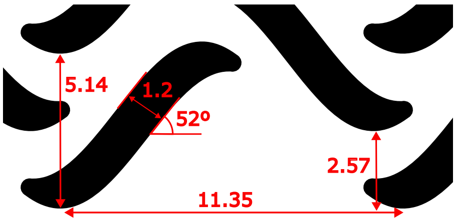


**Figure 4:** Dimensions of the S-shaped fins in mm. Out of plane height of 1.41 mm, giving a hydraulic diameter of 1.65 mm.

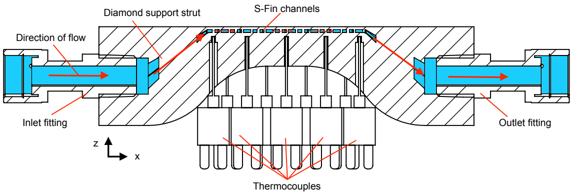


**Figure 5:** Cross-sectional view of the steel test piece with thermocouples installed.

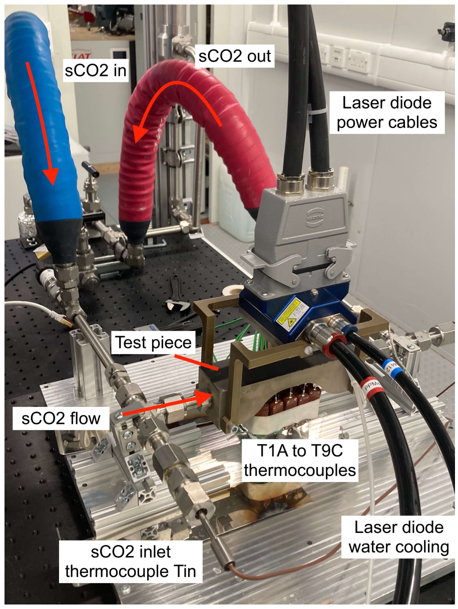


**Figure 7:** View of the experimental test rig.

together. Additive manufacturing was used in this study to reduce cost and manufacturing time. The test piece, as illustrated in Fig. 5, was made out of 316 stainless steel. The part was designed in conjunction with Finite Element mechanical simulations to check the structural integrity. Threads were tapped for the fittings to the rig.

A significant limitation of additive manufacture is the minimum feature size of approximately 1.2 mm. The current authors decided to scale the geometry in [9] by a factor of 1.5 to ensure that the geometry was accurate and the surface smooth, with a calculated surface roughness $R_a/D_h$ of $4.16 \times 10^{-3}$. The resulting fin dimensions are given in Fig. 4.

The test piece was instrumented with 23 thermocouples as shown in Fig.s 5 and 6: 8 K-Type with a base uncertainty of ±1 °C, and 15 Class 1 T-Type with a base uncertainty of ±0.25 °C. Blind holes enabled the thermocouples to non-invasively measure the temperature 2 mm below the fluid path. Thermocouples were were fixed using a paste[1] with a thermal conductivity of 2.30 W/mK.

Testing occurred at OLAHF [18], the rig is shown in Fig. 7. Outside the test piece, two T-type thermocouples (±0.5 °C) measure the $sCO_2$ temperature at inlet and outlet. Two side channel pumps[2] operating in a parallel configuration drive the flow to the test piece in combination with throttle valves downstream of their outlets. Pump motor frequency was varied to fine-tune the flow rate and ensure its consistency once the throttle valves were set. Loop pressures were set and maintained by an array of piston accumulators connected to a standard 230 bar nitrogen ($N_2$) bottle. Pressures were monitored at the inlet and outlet using industrial pressure transducers[3], with an operating range of 0 to 160 bar and a nominal accuracy of ±0.8 bar full span [20]. The flow rate was measured by a Coriolis flow meter[4] with a range of 0 to 100 kg/min and a base uncertainty of ±0.2%.

Heat input was provided by one of the facility's laser modules[5]. This allowed for continuous operation, allowing temperatures to reach steady state values. These conditions closely match the radiative heat flux and operating temperatures experienced by the blanket in fusion reactors.

To ensure even and known absorption of the applied laser to the test piece the top surface was coated with high-emissivity paint[6], which has previously been calibrated for use in this facility to have an absorption coefficient $\alpha$ of 0.87 ± 0.012 [18].

The range of input parameters are summarised in Table 1. Experiments were all performed at an $sCO_2$ pressure of 80 bar, at three different inlet $sCO_2$ temperatures (20, 24, and 28 °C), three different laser heat fluxes (0.1, 0.5, and 1.0 $MW/m^2$), and two different $sCO_2$ flow rates (0.05 and 0.09 kg/s). For each of the 18 test conditions, outlet values were allowed to stabilise before taking readings.

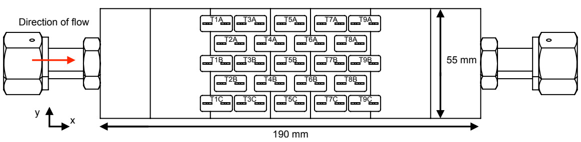


**Figure 6:** Underside of the steel test piece, with labelled thermocouples.

[1] AS1802 SILCOTHERM©
[2] Dickow Pumpen WPM25 [19]
[3] Swagelok© model PTI-S-AG160
[4] Rheonik RHM12L [19]
[5] 1.2 kW VCSEL laser diode PPM412 Type [21]
[6] Aremco HiE-Coat™ 840-CM [22]


DOI: 10.17185/duepublico/83302

| Parameter | Symbol | Values |
|---|---|---|
| Pressure | $P_{in}$ | 80 bar |
| Temperature | $T_{in}$ | 20, 24, 28 °C |
| Mass flow rate | $\dot{m}$ | 0.05, 0.09 kg/s |
| Heat flux | $q_{in}$ | 0.1, 0.5, 1.0 $MW/m^2$ |

**Table 1:** Range of experimental inputs for the $sCO_2$.

## 3. DATA REDUCTION

A variety of numerical techniques were used to interpret the experimental data. Fig. 8 shows how these fit together. Ray tracing was used to determine the two-dimensional heat profile on the top surface of the test piece. This profile was used as a boundary condition for the computational fluid dynamics (CFD) and Finite Element model (FE). The dimension perpendicular to the direction of flow was integrated out to give a one dimensional boundary profile to the thermal resistance network (TRN). The experimental temperatures were used as an input to the TRN, a simplified two-dimensional model of the test piece, and the unknown heat transfer coefficient was varied to minimise error with the experimental temperatures.

The temperatures at the positions of the thermocouples in the CFD did not match the experimental temperatures, see Section 4.2., so an FE model was used to expand the simulated region to include more of the test piece. The heat transfer distribution from the CFD was taken as an input and scaled until the temperature at one thermocouple matched the simulation well.

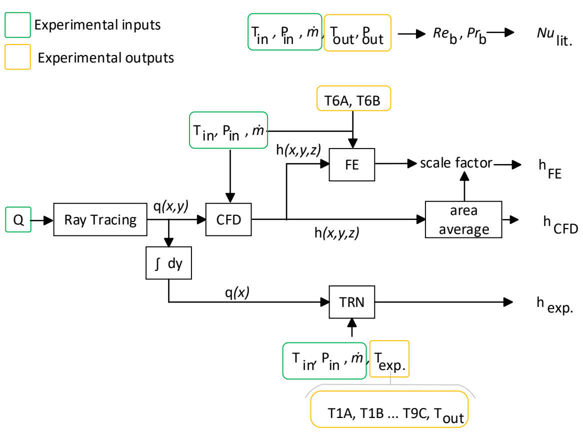


**Figure 8:** The interaction between the various numerical methods.

### 3.1. Ray Tracing

Ray tracing analysis was used to predict the incoming heat flux from the laser module. Analysis was performed in LightTools version 8.5.0 on a CAD-generated representation of the experimental setup in Fig. 7, resulting in a numerical representation of the applied experimental heat flux. Previous work [23] has shown ray tracing to accurately reproduce experimentally applied heat fluxes (to within ±1.5%, [18]). Here, a total of 10 million rays were modelled which impact a surface mesh of 0.5 x 0.5 mm resolution. Ray paths were calculated using a Monte Carlo simulation method, yielding a heat flux distribution that was scaled by the test piece coating's absorption coefficient ($\alpha = 0.87$, see Section 2.) and shown in Fig. 9. For the thermal resistance network, see Section 3.4., the heat flux distribution was integrated with respect to $y$, giving a one-dimensional heat profile $q(x)$. These distributions were appropriately scaled for the two other heat fluxes investigated in this study by the ratio of applied to peak power. The laser module was fixed to the test piece using brackets made of ABS to ensure consistency across the numerical and experimental setups.

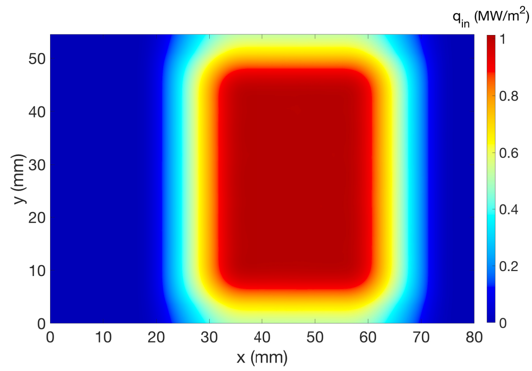


**Figure 9:** Two dimensional heat profile from ray tracing.

### 3.2. Computational Fluid Dynamics

Computational Fluid Dynamics (CFD) simulations were performed to understand the internal heat transfer profile. A conjugate CFD study was performed in Ansys CFX 2022 R2 [24], with meshing of the part performed in ICEM 2022 R2 [25]. Only the region of fins was simulated, to limit the number of nodes, as shown in Fig. 10. This region extends across the full extent of S-shaped fins, as well as from the heated surface down to the plane the thermocouple measure the temperatures of.

In other work by [23], it was found SST turbulence models matched the experimental supercritical $CO_2$ data better than $k-\omega$ or $k-\epsilon$.

HTC values were derived from an area average of the simulated heat flux into the sCO2 divided by the simulated wall temperature minus a reference temperature, here manually chosen as the bulk fluid temperature (however the reference temperature did not have a strong influence on apparent HTCs). Nu number was calculated from this HTC, and the fluid properties at the bulk fluid temperature, and pressure (average of inlet pressure of 80 bar and outlet simulated pressure).

A mesh sensitivity study was performed, to see whether the solutions were invariant to general mesh density and prism layer density. A mesh density of 20 million elements gives within 2% of the finer mesh pressure drop across the test piece in half the simulation time, which is sufficient for this study, as shown in Table 2. This resulted in a general side length of 0.2 mm being chosen. The $sCO_2$ temperature


DOI: 10.17185/duepublico/83302

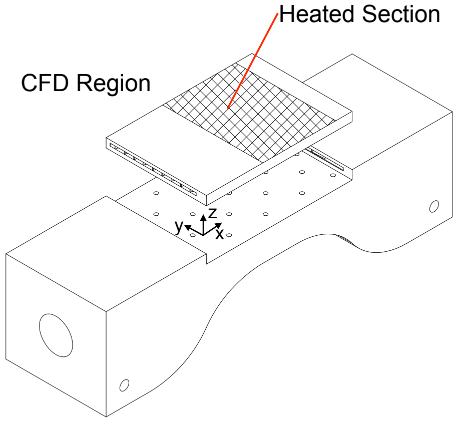


**Figure 10:** Diagram to show the region CFD was performed on in relation to the whole test piece.

changes and average HTCs are independent of the number of prism layers, Table 3, so sufficient prism layers were used to keep a $y^+$ below 1. 14 prism layers were used, with a maximum height of 0.08 mm and a growth ratio of 1.2.

| Fineness | No. elements (million) | Simulation time (hours) | $\Delta P$ (Pa) | Min. side length (mm) |
|---|---|---|---|---|
| Coarse | 6 | 1.5 | 571 | 0.3 |
| Medium | 20 | 10 | 540 | 0.19 |
| Fine | 30 | 17 | 530 | 0.115 |

**Table 2:** General mesh density sensitivity study.

| No. prism layers | $\Delta T$ (°C) | $h$ (kW/m$^2$) |
|---|---|---|
| 8 | 41.07 | 1.80124 |
| 10 | 41.039 | 1.80299 |
| 12 | 41.1407 | 1.79641 |
| 14 | 41.1956 | 1.80253 |
| 16 | 41.1425 | 1.80566 |

**Table 3:** Prism layer sensitivity study.

## 3.3. Finite Element model

A Finite Element model (FE) was developed to predict the test section temperature for a given heat transfer coefficient distribution. This took the heat transfer distribution on the internal surfaces from CFD and scaled it by a specific factor. Outside of this region, a uniform, average value was applied. The whole test piece was simulated in this conduction model, as well as losses to the air including radiative losses and convective losses to the air. The scaling factor was adjusted until the temperatures at the centre of the heated region matched the experimental values (T6A and T6B in Fig. 6, as these were the most sensitive temperatures to the test conditions). A mesh sensitivity study was performed, and gave temperature values within 0.1 °C for the mesh sizes between 0.01 – 0.1 mm and so results are assumed to be mesh invariant.

## 3.4. Thermal Resistance Network

A thermal resistance network model (TRN) was used to determine heat transfer coefficients in the test piece using experimental temperatures. An unknown heat transfer coefficient $h$ was varied to minimise the error between experimental and simulated temperatures yielding an estimate of the experimental value of heat transfer coefficient $h_{\text{exp.}}$. This eliminates the need to directly measure the internal $sCO_2$ temperatures, which is difficult to do without disturbing the flow field. The following sections detail specific model properties used in this study.

### From heat transfer coefficient to simulated temperatures

From CFD simulations, temperature gradients perpendicular to the flow were found to be much smaller than gradients in the direction of the flow ($\left|\frac{\partial T}{\partial y}\right| \ll \left|\frac{\partial T}{\partial x}\right|$). Therefore transverse temperatures were averaged (with respect to $y$) and the network was sized to represent a characteristic 2D slice of the test piece. The various heat flows incorporated are shown in Fig. 11 for one slice in the $x$ direction. The incoming radiative heat $Q_{\text{in}}$ from the lasers was found from ray tracing (Section 3.1.), and directly heats the top of the steel, the top line of nodes. Re-radiation back from the steel $Q_{\text{r}}$, given by the Stefan-Boltzman equation [26], has been included, as some of the steel temperatures can reach upwards of 200 °C. The other external heat flow on the top surface is that of natural convection to the ambient air. The heat transfer coefficient for this $h_{\text{a}}$ was chosen to be constant at 5 W/m$^2$. Whilst a correlation could be used for this, even at the highest temperatures the maximum local $h_{\text{a}}$ expected would be 10 W/m$^2$, and the magnitude of heat flux was small enough for this difference to be ignored as convection losses to the air were found to be typically 3 orders of magnitude smaller than conduction into the steel. Heat losses to the air on the sides and bottom of the test piece were negligible. Extra steel below the level of the thermocouples were neglected as heat flows in this area were small.

The conductivity of the steel ($k_{\text{s}}$) was interpolated based on previous time-step temperature using data from [27]. For conduction inside the steel, the conduction constant was calculated based on the averaged temperature between adjacent nodes. A similar method was employed for the $sCO_2$, which has a dependence on both temperature and pressure, and much more pronounced variations. Values for the properties of $sCO_2$ were taken from NIST [7]. Conduction in the $sCO_2$ was found to have a very small effect (< 1 % of other heat fluxes).

The friction factor was calculated from correlations found in [9], and from this the pressure change in the $sCO_2$, although it was found to be small enough so as not to affect the flow properties. The mass flow rate adds a term that is treated similarly to a heat flux, from the change in enthalpy into and out of a node, $Q = \dot{m}\Delta i$, represented in Fig. 11 by $\dot{m}$. The heat transfer between the steel and the $sCO_2$


DOI: 10.17185/duepublico/83302

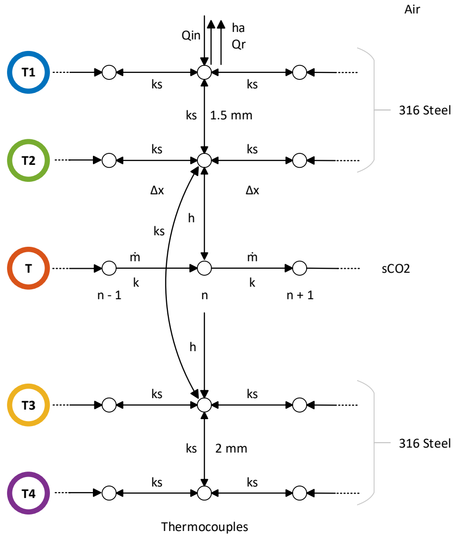


**Figure 11:** Node diagram for the thermal resistance network showing heat flows.

was represented by the convective coefficient $h$, an input to the TRN. Temperatures were predicted iteratively with an adapted Newton-Raphson scheme to achieve convergence.

### From experimental temperatures to heat transfer coefficient

The heat transfer coefficient $h$ between the $sCO_2$ and the steel walls was varied to minimise a weighted least square error, given by equation 1, between the experimentally measured temperatures and those estimated by the TRN. The measured inlet temperature was taken to be the inlet $sCO_2$ temperature to the model. The experimental temperatures $T_{\text{exp. j}}$ were an arithmetic average of the available measured values at that distance along the direction of flow, e.g. $T_{\text{exp. 3}} = \frac{T_{3A}+T_{3B}+T_{3C}}{3}$. Weightings were used to account for the different uncertainty of the different thermocouples, $\delta T_{\text{exp. j}}$. The value of $h$ that minimised the error, $h_{\text{exp.}}$, was found through a golden-section line search algorithm.

$$h_{\text{exp.}} = \arg\min_{h} \sqrt{\frac{\sum_{\text{j}}^{N_{\text{exp.}}} \frac{1}{\delta T^2_{\text{exp. j}}} (T_{\text{j}}(h) - T_{\text{exp. j}})^2}{N_{\text{exp.}}}} \tag{1}$$

Uncertainty analysis was performed by a Kline-McClintock style analysis as proposed by [28], and shown in equation 2. The sensitivity of $h$ wrt. each experimental variable $j$ (where $j$ is any of the experimental inputs like $T_{\text{in}}$, $P_{\text{in}}$ etc...) ($\frac{\partial h}{\partial j}$) is approximated by a finite-difference method, where the TRN is run for very slightly different values of the experimental variables. These sensitivities are then multiplied by the uncertainty in that variable, $\delta j$, and the square of the sum of these is added to find the uncertainty in $h_{\text{exp.}}$, $\delta h$.

$$\delta h^2_{\text{exp.}} = \sum_j \left(\frac{\partial h}{\partial j}\delta j\right)^2, \forall j \in [T_{\text{in}}, P_{\text{in}}, q, \dot{m}, T_{\text{out}}, T_{\text{exp. 1}} - T_{\text{exp. 9}}] \tag{2}$$

## Model validation

The TRN output $h_{\text{exp.}}$ was found to be independent of both mesh density above a mesh density of 1 slice/mm and initialisation temperatures 10 °C < $T_{\text{init}}$ < 40 °C, as shown in in Fig. 12.

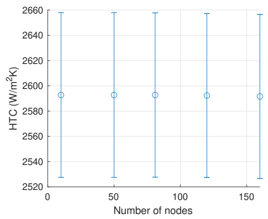


**(a)** Dependence of HTC $h$ on number of nodes.

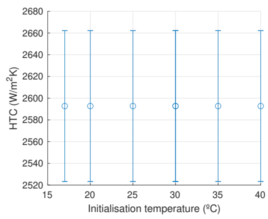


**(b)** Dependence of HTC $h$ on initialisation temperature.

**Figure 12:** Sensitivity analysis for the method of finding the heat transfer coefficient $h$.

The TRN was validated against experimental results in the literature, as shown in Table 4. The correlation in [9] was developed for a counter-current heat exchanger with two flows of $sCO_2$ on both the hot and cold sides. Modifications to the resistance network were made to reflect this, and, using typical HTC values given in [9], the TRN values agree with the experimental temperatures.

| Location | Experimental value (°C) | Nominal TRN value (°C) | Min. (°C) | Max. (°C) |
|---|---|---|---|---|
| Cold side inlet | 48.27 | set at 48.27 | N.A. | N.A. |
| Hot side inlet | 120.42 | set at 120.42 | N.A. | N.A. |
| Cold side outlet | 111.59 | 112.129 | 110.940 | 113.281 |
| Hot side outlet | 51.10 | 52.78 | 51.18 | 53.53 |

**Table 4:** Validation of the thermal resistance network, using the nominal correlation given in [9], and the error bounds on it to get minimum and maximum predicted temperatures and comparing these to experimental values.

## 4. RESULSTS AND DISCUSSION

This section will cover the various simulations (CFD, FE, and TRN) and how they relate both to the experimental data in this study, and literature values.

### 4.1. Thermal Resistance Network Results

This section covers the results from the Thermal Resistance Network. The TRN minimises the error between its temperature estimates and the experimental values for a representative slice of the heat exchanger by varying the HTC.

Fig. 13 shows the experimental HTC $h$exp. from the TRN against inlet $sCO_2$ temperature $T_{\text{in}}$, for different mass flow


DOI: 10.17185/duepublico/83302

rates $\dot{m}$ and heat fluxes $q_{\text{in}}$. HTC is larger for higher mass flow rates. Relationships with inlet temperature and applied heat flux are less obvious.

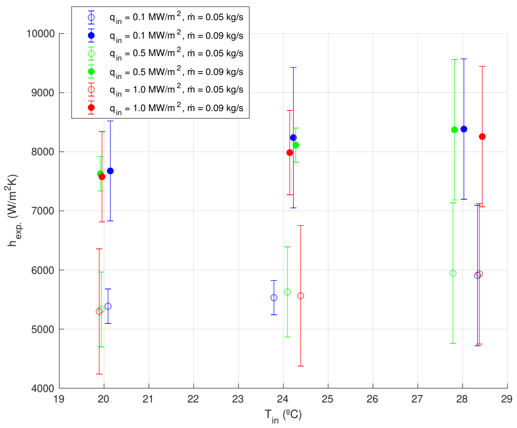


**Figure 13:** Experimental heat transfer coefficient from the TRN plotted against inlet $sCO_2$ temperature.

Non-dimensional numbers allow comparison to other experimental data. Using the $sCO_2$ bulk fluid properties to normalise HTC to Nu, and flow speed to Re, yields Fig. 14 which shows experimental Nusselt number against Reynolds number. As expected, higher Re flows have higher Nusselt numbers. Trend-lines for the literature correlation in [9] at the extreme Pr values in the present study of 2 and 3.5 are added. All points lie in the expected range, between the two lines for the literature correlation.

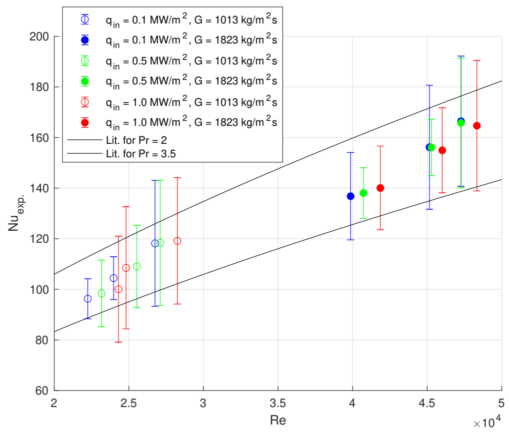


**Figure 14:** Experimental Nusselt number from the TRN plotted against Reynolds number of the experiment.

To allow better comparison with the correlation in the literature, the next figures use a ratio of the experimental Nu in the present study with the value predicted using the correlation [9]. Fig. 15 shows the experimental Nu from the TRN, normalised by the expected value from the correlation given in [9], against Reynolds number, for different mass fluxes $G$ and heat fluxes $q_{\text{in}}$.

For all data points, the error bars extend over 1. This means that the correlation holds at the higher heat fluxes and Reynolds numbers of this experimental study, as a value of 1 would make $\text{Nu}_{\text{exp.}} = \text{Nu}_{\text{lit.}}$. It is worth noting that the higher heat flux data points tend to be slightly lower, possibly indicating a minor deterioration in heat transfer, however this is smaller than experimental uncertainty .

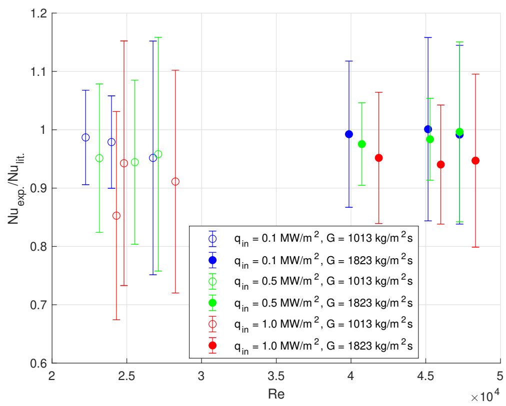


**Figure 15:** Experimental Nusselt number from the TRN divided by the expected value from the correlation in [9], plotted against Reynolds number of the experiment.

Fig. 16 shows these values against the bulk temperature of the fluid $T_{\text{b}}$, normalised by the pseudo-critical temperature at that pressure, $T_{\text{pc}}$, which is the temperature at which specific heat capacity $C_{\text{p}}$ reaches a maximum at this pressure. This study is only for $sCO_2$in the sub-critical temperature range owing to limitations on the amount the volume of experimental loop could change, therefore $\frac{T_{bulk}}{T_{pc}}$ is always < 1. Once again, the correlation is shown to hold at higher heat fluxes than previously tested in the literature.

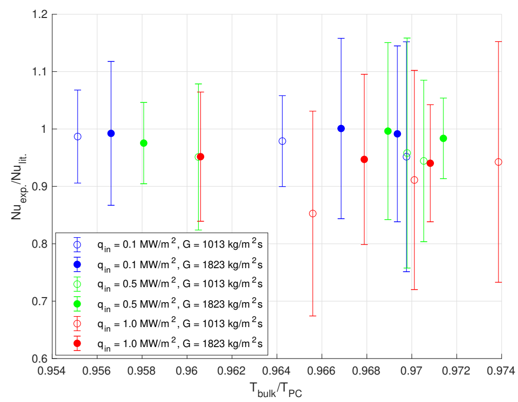


**Figure 16:** Nusselt number from the TRN divided by the expected value from the correlation in the literature, plotted against the bulk temperature of the experiment divided by the pseudo-critical temperature.

The correlation holds at the higher heat flux and Reynolds number. Table 5 compares the Reynolds number, Prandtl number, and heat flux ranges for which the correlation was proposed, in [9], and tested in the present study. As the corre-


DOI: 10.17185/duepublico/83302

lation holds at heat fluxes as high as 1 $\mathrm{MW/m^2}$, it shows that S-shaped fins are an effective MCHE geometry for nuclear fusion applications.

| Reynolds no. Range | Prandtl no. range | Heat Flux |
|---|---|---|
| [9] | | |
| $3.5\times10^3 < \mathrm{Re} < 2.3\times10^4$ | $0.75 < \mathrm{Pr} < 2.2$ | $q < 0.05\,\mathrm{MW/m^2}$ |
| Present | | |
| $2.2\times10^4 < \mathrm{Re} < 4.8\times10^4$ | $2.5 < \mathrm{Pr} < 3.5$ | $q < 1\,\mathrm{MW/m^2}$ |

**Table 5:** Range of correlations.

## 4.2. Computational Fluid Dynamics Results

This section covers the results from CFD simulations.

Fig. 17 compares the results from CFD to the literature correlation in [9]. The CFD was found to over-estimate the HTC by about a factor of two, although this was dependent both on the Reynolds number and the heat flux.

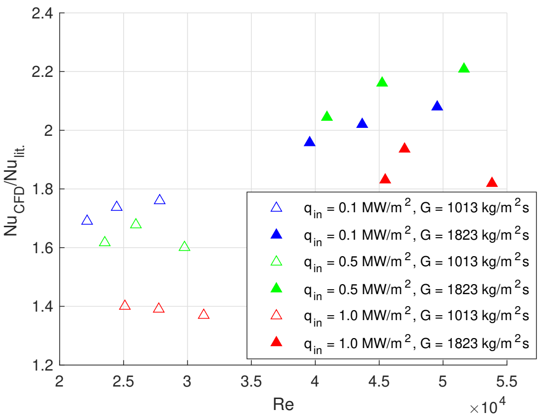


**Figure 17:** Nusselt number from CFD divided by the expected value from the correlation in the literature, plotted against Reynolds number.

In addition to over-estimating the HTC, the CFD also over-estimates the $sCO_2$ and steel temperatures at the level of the thermocouples, Fig. 18 and Fig. 20 respectively. The TRN accurately predicts the exit bulk temperature of the $sCO_2$, but under-estimates the steel temperatures.

As the TRN represents an average slice through the test piece, it only has one temperature value at each point along the flow. CFD is a 3D simulation, and so yields temperatures at different points tranverse to the flow. Fig. 19 shows the underside view of the test-piece, and the colour-coding for the different $y$ positions of temperature measurements.

Fig. 20 shows the temperatures at the level of the thermocouples in the steel both from experimental data, and predicted by the TRN and CFD. As with the $sCO_2$ temperatures, CFD over-estimates. The CFD lines show variation from the position of the S-shaped fins and cooling channels, which is more pronounced in the lines closer to the edge of the test-piece (pink and purple).

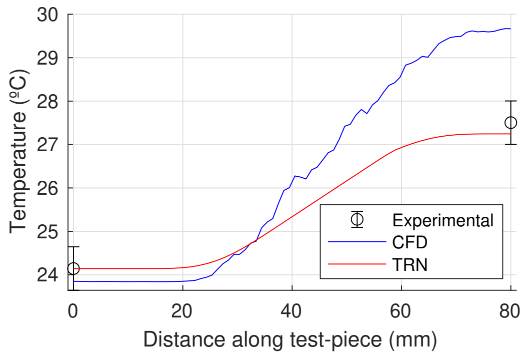


**Figure 18:** Temperature distribution in the bulk of the $sCO_2$ as predicted by the TRN, CFD, compared to the experimental data for an inlet heat flux of 1 $\mathrm{MW/m^2}$, and mass flow rate of 0.09 kg/s.

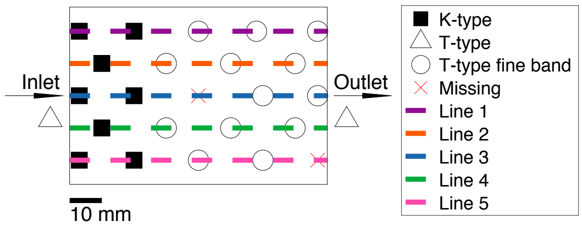


**Figure 19:** Diagram of the underside of the test-piece, showing thermocouple locations. Colour-coding of the different $y$ cross-sections.

The CFD simulations do not accurately predict HTC values, reinforcing the need for experimental results, however some temperature predictions were close. There does not appear to be a simple trend that could be easily corrected. This may be because of the large fluid property variations in supercritical fluids, resulting in simulations not matching experimental reality. Alternative methods like Large Eddy Simulations are better at accounting for these variations and so tend to be more accurate for supercritical fluids, however the large computational requirements meant they were out of the scope of this project.

## 4.3. Finite Element Model Results

To improve upon the estimates from CFD, a FE model used the distribution from CFD and scaled it by a factor until some central values matched the experimental values, as well as expanding the simulated region to include more of the test piece, as described in the Section 3.3.. This section covers the results from the FE model.

Fig. 21 compares the temperature in the steel at the level of the thermocouples between both the FE model, the TRN, and the experimental data. The TRN is minimising the error between its temperature estimates and the experimental values for a representative slice of the heat exchanger by varying the HTC. The FE model uses a scaled version of the CFD HTC profile to match the experimental temperatures at the middle of the test piece.


DOI: 10.17185/duepublico/83302

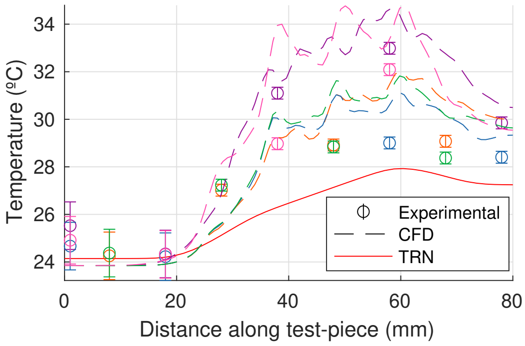


**Figure 20:** Temperature distribution in the steel 2 mm below the finned region as predicted by the TRN, CFD, compared to the experimental data for an inlet heat flux of 1 $MW/m^2$, and mass flow rate of 0.09 kg/s. Different colours refer to different $y$ position of thermocouples in Fig. 6 and 19.

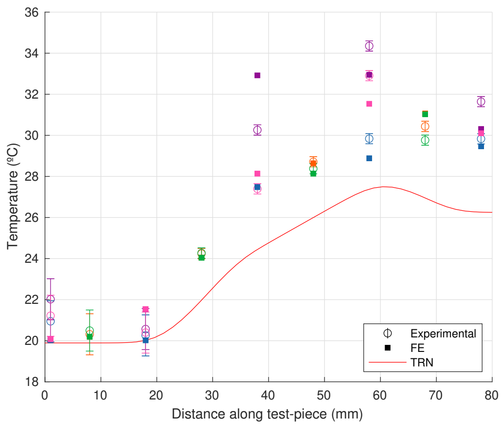


**Figure 21:** Comparison of the temperatures predicted by the FE model, the temperatures from the TRN, and experimental values. Different colours refer to different $y$ position of thermocouples in Fig. 6 and 19.

The FE model matches the experimental temperatures well. The TRN underestimates the temperatures, and does not estimate temperature variation in the direction perpendicular to the flow as it is a two-dimensional model.

The temperatures match well, a sign that the HTC distribution from CFD is accurate, although the HTC had to be increased further by a factor of approximately 3, meaning that the FE model over-estimated HTCs by a factor of 5.

Fig. 22 compares the temperatures from the FE model to the experimental results. The different colour series refer to corresponding lines of thermocouples along the test piece, as in Fig. 6. Odd A being the left most, Odd B being the central, and Odd C being the right most relative to the direction of flow. The temperatures from the FE model mostly follow the experimental temperatures, but lie outside the ±1 or ±0.25 °C uncertainties of the thermocouples.

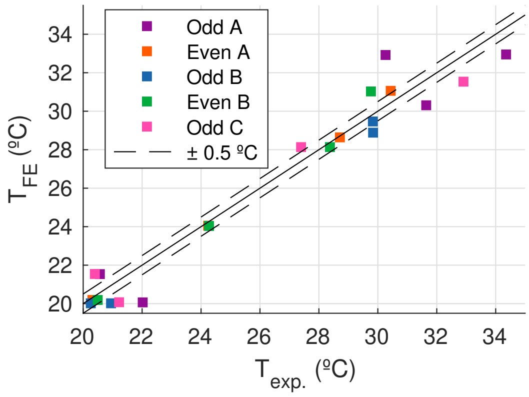


**Figure 22:** Temperatures predicted by the FE model vs the experimental values. Different colours refer to different $y$ position of thermocouples in Fig. 6 and 19.

A simple multiplicative factor on the HTC distribution from CFD to match temperature values in one experimental case did predict well for other cases, indicating that using one experiment as a calibration for the CFD-FE method could be used to predict temperatures in other experimental cases, however could not easily be used to predict HTCs without any experiments.

## 5. CONCLUSIONS

This paper aimed to investigate the used of S-shaped fin MCHEs and $sCO_2$ for fusion wall cooling. As heat transfer correlations for supercritical fluids do not necessarily carry over to higher heat fluxes, this paper experimentally verified that proposed in [9] held at much higher heat fluxes.

CFD simulations were performed at the same conditions from the experimental study. These over-estimated both the experimental temperatures, and heat transfer coefficients. By scaling the CFD-generated HTC profile in a finite-element model, the temperatures matched well. This indicates that the profile is accurate, however the magnitude of HTC did not match either the present study experimental values or the literature values. Temperatures could be predicted after using an experiment to calibrate the scale factor needed, but these methods could not be used to predict HTC values.

A thermal resistance network was used to estimate the HTCs. These matched correlations in the literature at these elevated heat fluxes of 1 $MW/m^2$, as in the blanket of fusion reactors. This suggests $sCO_2$ cooling of S-fin MCHEs is a possible option for cooling the blanket of magnetic confinement fusion reactors.

## References

[1] M. Kikuchi and K. Lackner, *Fusion Physics*. International Atomic Energy Agency (IAEA): IAEA, 2012.

[2] A. Raffray and M. Merola, "Overview of the design and r&d of the iter blanket system," *Fusion Engineering and Design*, vol. 87, no. 5, pp. 769–776, 2012. Tenth


DOI: 10.17185/duepublico/83302

International Symposium on Fusion Nuclear Technology (ISFNT-10).

[3] M. T. White, G. Bianchi, L. Chai, S. A. Tassou, and A. I. Sayma, "Review of supercritical co2 technologies and systems for power generation," *Applied Thermal Engineering*, vol. 185, p. 116447, 2021.

[4] J. Jackson, "Fluid flow and convective heat transfer to fluids at supercritical pressure," *Nuclear Engineering and Design*, vol. 264, pp. 24–40, 2013. SI:NURETH-14.

[5] S. R. Pidaparti, M. H. Anderson, and D. Ranjan, "Experimental investigation of thermal-hydraulic performance of discontinuous fin printed circuit heat exchangers for supercritical co2 power cycles," *Experimental Thermal and Fluid Science*, vol. 106, pp. 119–129, 2019.

[6] Z. Zhao, Y. Zhang, X. Chen, X. Ma, S. Yang, and S. Li, "Experimental and numerical investigation of thermal-hydraulic performance of supercritical nitrogen in airfoil fin printed circuit heat exchanger," *Applied Thermal Engineering*, vol. 168, p. 114829, 2020.

[7] R. Span and W. Wagner, "A new equation of state for carbon dioxide covering the fluid region from the triple-point temperature to 1100 k at pressures up to 800 mpa," *Journal of Physical and Chemical Reference Data*, vol. 25, no. 6, pp. 1509–1596, 1996.

[8] B. Agostini, M. Fabbri, J. E. Park, L. Wojtan, J. R. Thome, and B. Michel, "State of the art of high heat flux cooling technologies," *Heat Transfer Engineering*, vol. 28, no. 4, pp. 258–281, 2007.

[9] T. L. Ngo, Y. Kato, K. Nikitin, and T. Ishizuka, "Heat transfer and pressure drop correlations of microchannel heat exchangers with s-shaped and zigzag fins for carbon dioxide cycles," *Experimental Thermal and Fluid Science*, vol. 32, no. 2, pp. 560–570, 2007.

[10] S. K. Mylavarapu, X. Sun, R. E. Glosup, R. N. Christensen, and M. W. Patterson, "Thermal hydraulic performance testing of printed circuit heat exchangers in a high-temperature helium test facility," *Applied Thermal Engineering*, vol. 65, no. 1, pp. 605–614, 2014.

[11] G. Tanda, "Heat transfer and pressure drop in a rectangular channel with diamond-shaped elements," *International Journal of Heat and Mass Transfer*, vol. 44, no. 18, pp. 3529–3541, 2001.

[12] S. Yoon, H. C. No, and G. B. Kang, "Assessment of straight, zigzag, s-shape, and airfoil pches for intermediate heat exchangers of htgrs and sfrs," *Nuclear Engineering and Design*, vol. 270, pp. 334–343, 2014.

[13] N. Tsuzuki, Y. Kato, and T. Ishiduka, "High performance printed circuit heat exchanger," *Applied Thermal Engineering*, vol. 27, no. 10, pp. 1702–1707, 2007. Heat transfer and sustainable energy technologies.

[14] N. Tsuzuki, Y. KATO, K. NIKITIN, and T. ISHIZUKA, "Advanced microchannel heat exchanger with s-shaped fins," *Journal of Nuclear Science and Technology*, vol. 46, no. 5, pp. 403–412, 2009.

[15] M. Utamura, K. Nikitin, and Y. Kato, "A generalized mean temperature difference method for thermal design of heat exchangers," *International Journal of Nuclear Energy Science and Technology*, vol. 4, 03 2008.

[16] K. Nikitin, Y. Kato, and T. Ishizuka, "Icone15-10826 experimental thermal-hydraulics comparison of microchannel heat exchangers with zigzag channels and s-shaped fins for gas turbine reactors," *The Proceedings of the International Conference on Nuclear Engineering (ICONE)*, vol. 2007.15, pp. ICONE1510–ICONE1510, 04 2007.

[17] C. Zeng, Y. Song, X. Zhou, F. Zhang, M. Jiao, M. Liu, and H. Gu, "Experimental study on heat transfer and pressure drop characteristics in a microchannel heat exchanger assembly with s-shaped fins," *Applied Thermal Engineering*, vol. 210, p. 118406, 2022.

[18] Z. Jackson, A. Bebb, P. Ireland, and J. Nicholas, "The Oxford Laser Heating Facility." unpublished, 2023.

[19] Rheonik, "RHM12L Coriolis flow meter," 2024.

[20] Swagelock, "Industrial Pressure Transducers, model PTI-S-AG160," 2024.

[21] TRUMPF Photonic Components GmbH, "VCSEL Heating Systems," 2023.

[22] Aremco, "High temperature high emissivity coatings," 2023.

[23] Z. Jackson, "Characterising the Behaviour of Supercritical CO2 at High-Heat Flux Conditions." unpublished, 2023.

[24] Ansys, "CFX 2022 R2," 2023.

[25] Ansys, "ICEM CFD 2022 R2," 2023.

[26] L. Boltzmann, "Ableitung des stefan'schen gesetzes, betreffend die abhängigkeit der wärmestrahlung von der temperatur aus der electromagnetischen lichttheorie," *Annalen der Physik*, vol. 258, no. 6, pp. 291–294, 1884.

[27] A. Iron and S. Institute, *High-temperature characteristics of stainless steel - a designers' handbook. Series no. 9004*. Toronto, Ont. : Nickel Institute, 2020., 2020.

[28] R. Moffat, "Describing the uncertainties in experimental results," *Experimental Thermal and Fluid Science*, vol. 1, no. 1, pp. 3–17, 1988.


DOI: 10.17185/duepublico/83302

## ANNEX A

## FIN GEOMETRY DATA

The S-Fins are sinusoids generated by the two equations 3 and 4, with the parameters shown in Table 6. A radius between the sinusoidal curves of 0.2 mm was used. Fins in the next row up in the $y$ direction are shifted up by pitch $p_y$. Fins in the next row across in the $x$ direction are mirrored and only shifted by $p_x/2$, fins in the row after that are facing the same way as the original set, and $p_x$ along from the original. Fig. 23 shows three fins to scale, forming the start of the pattern.

The side walls were chosen to be purely sinusoidal, with a wavelength equal to the $x$ direction pitch $p_x$. Experiments were designed so that edge effects were a small portion of the finned region.

$$y_{\text{top}} = a * sin((x + b) * c) + d \tag{3}$$

$$y_{\text{bot}} = a * sin((x - b) * c) - d \tag{4}$$

| Variable | Description | Value | Units |
|---|---|---|---|
| $f$ | Fin angle | 52 | ° |
| $l$ | Fin Length | 7.2 | mm |
| $w$ | Fin width | 1.2 | mm |
| $p_x$ | Pitch in $x$ direction | 11.35 | mm |
| $p_y$ | Pitch in $y$ direction | 5.14 | mm |
| $z$ | Out of page height | 1.41 | mm |
| $r$ | Fin tip radius | 0.2 | mm |
| $a$ | Sinusoid amplitude | 2.274 | mm |
| $b$ | Sinusoid phase offset | 0.447 | mm |
| $c$ | Sinusoid wavelength | 0.5628 | rad/mm |
| $d$ | Sinusoid offset | 0.4025 | mm |

**Table 6:** Parameters for the S-Fin geometry.

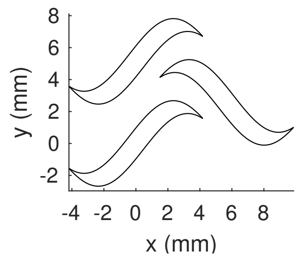

**Figure 23:** S-Fin geometry.


DOI: 10.17185/duepublico/83302

**DOI:** 10.17185/duepublico/83302
**URN:** urn:nbn:de:hbz:465-20250428-090438-6